NeuroImage 154 (2017) 92–105

Contents lists available at ScienceDirect

NeuroImage

journal homepage: www.elsevier.com/locate/neuroimage

Analysis and correction of field fluctuations in fMRI data using field monitoring

Saskia Bollmann[a,*,1], Lars Kasper[a,b,1], S. Johanna Vannesjo[a,2], Andreea O. Diaconescu[b], Benjamin E. Dietrich[a], Simon Gross[a], Klaas E. Stephan[b,c,d], Klaas P. Pruessmann[a]

[a] Institute for Biomedical Engineering, ETH Zurich and University of Zurich, 8092 Zurich, Switzerland
[b] Translational Neuromodeling Unit (TNU), Institute for Biomedical Engineering, University of Zurich and ETH Zurich, 8032 Zurich, Switzerland
[c] Wellcome Trust Centre for Neuroimaging, University College London, London WC1N 3BG, UK
[d] Max Planck Institute for Metabolism Research, 50931 Cologne, Germany

ARTICLE INFO

Keywords:
fMRI
Echo-planar imaging
Field fluctuations
Physiological noise
SFNR
Magnetic field monitoring

ABSTRACT

This work investigates the role of magnetic field fluctuations as a confound in fMRI. In standard fMRI experiments with single-shot EPI acquisition at 3 Tesla the uniform and gradient components of the magnetic field were recorded with NMR field sensors. By principal component analysis it is found that differences of field evolution between the EPI readouts are explainable by few components relating to slow and within-shot field dynamics of hardware and physiological origin. The impact of fluctuating field components is studied by selective data correction and assessment of its influence on image fluctuation and SFNR.

Physiological field fluctuations, attributed to breathing, were found to be small relative to those of hardware origin. The dominant confounds were hardware-related and attributable to magnet drift and thermal changes. In raw image time series, field fluctuation caused significant SFNR loss, reflected by a 67% gain upon correction. Large part of this correction can be accomplished by traditional image realignment, which addresses slow and spatially uniform field changes. With realignment, explicit field correction increased the SFNR on the order of 6%.

In conclusion, field fluctuations are a relevant confound in fMRI and can be addressed effectively by retrospective data correction. Based on the physics involved it is anticipated that the advantage of full field correction increases with field strength, with non-Cartesian readouts, and upon phase-sensitive BOLD analysis.

1. Introduction

Functional MRI of the brain typically relies on time series of MR image data with suitable weighting, most commonly based on BOLD (blood-oxygen-level dependent) mechanisms (Bandettini et al., 1992; Ogawa et al., 1990). Brain activity and connectivity are inferred upon from the spatiotemporal signal structure of such time series. Any unrelated signal fluctuations act as confounds that limit the sensitivity of the technique.

Confounds in fMRI are of diverse origin (Murphy et al., 2013). In task-based studies all brain activity unrelated to the task is effectively a confound and its manifestation in fMRI data is often comprised in the notion of physiological noise. Confounds of physiological nature also include signal fluctuations due to respiration or heart rate variation (Chang et al., 2009; Birn et al., 2006; Chang and Glover, 2009), blood vessel pulsation (Mandeep et al., 1999), pulsatile blood flow and the associated subtle bulk motion of the head, as well as any other head motion (Power et al., 2012).

Further MR image fluctuations arise from imperfections of the instrumentation used and the electromagnetic fields involved. Regarding radiofrequency, the net gains of transmit and receive chains immediately affect the signal level of resulting data. Confounding gain changes can arise, e.g., from power amplifier fluctuations, instability of supply voltages, or changes in coil loading due to motion. Baseline and gradient magnetic fields, ranging from DC to few tens of kHz, fluctuate mostly due to imperfections of magnet and gradient hardware. However, low-frequency field perturbations also arise from the magnetic susceptibility of the subject in conjunction with physiological mechanisms, particularly with breathing (Pfeuffer et al., 2002; Raj et al., 2000; Van de Moortele et al., 2002) and, potentially, cardiovas-

* Corresponding author. Current address: Centre for Advanced Imaging, University of Queensland, 4072 Brisbane, QLD, Australia.
E-mail address: saskia.bollmann@cai.uq.edu.au (S. Bollmann).
[1] These authors contributed equally.
[2] Current Address: FMRIB Centre, Nuffield Department of Clinical Neurosciences, University of Oxford, Oxford, UK.

http://dx.doi.org/10.1016/j.neuroimage.2017.01.014
Accepted 6 January 2017
Available online 09 January 2017
1053-8119/ © 2017 Elsevier Inc. All rights reserved.

cular action (Gross et al., 2016; Pruessmann et al., 2011).

The present work focuses on this latter class of confounds related to magnetic field perturbations up to the audio-frequency range. Alterations of field strength change the Larmor frequency of nuclear spins and thus their phase accrual after excitation. Yet spin phase is also the carrier of spatial encoding in MRI. Therefore, field perturbations change how MR signal is depicted in resulting images. When the underlying field errors fluctuate over fMRI time series so do the depiction errors, which then act as confounds.

The form and magnitude of depiction errors caused by a given field perturbation depend strongly on the encoding strategy. The most common fMRI readout by far is single-shot 2D echo-planar imaging (EPI), which combines high spatiotemporal resolution with high SNR efficiency, relative robustness against motion, and sharper time assignment than segmented approaches (Bandettini et al., 1992; Mansfield, 1977). For considering the effects of field perturbation in single-shot EPI it is useful to distinguish slow field changes that are approximately static over each single-shot experiment (of typically several tens of ms) and higher-frequency field errors that vary within shots.

Slow field changes arise chiefly from magnet drift, temperature change of magnetised parts (Busch et al., 2014; Foerster et al., 2005), particularly of passive shims, and breathing (Pfeuffer et al., 2002; Raj et al., 2000; Van de Moortele et al., 2002; Windischberger et al., 2002). In single-shot EPI such slow-changing field offsets result primarily in image distortion by shifting image contents in the phase-encoding direction, by a distance proportional to the local field offset. To a smaller degree they also cause ghosting and blurring due to inconsistency of phase increments along odd and even k-space lines (Hennel, 1997). They strongly perturb the image phase, which however concerns fMRI only upon phase-sensitive data analysis (Calhoun et al., 2002; Rowe, 2005; Rowe and Logan, 2004), which is rarely performed to-date. Slow field fluctuations are commonly addressed by two strategies. At the acquisition stage, navigator readouts added to the sequence serve to constantly re-determine the global B_0 (Foerster et al., 2005; Hu and Kim, 1994; Pfeuffer et al., 2002; Splitthoff et al., 2007; Versluis et al., 2010; Ward et al., 2002) or, using a receiver array, a higher-order field model (Splitthoff and Zaitsev, 2009) for data correction. At the image processing stage, varying distortion is partly addressed by co-registration (Andersson et al., 2003, 2001; Ashburner and Friston, 2007; Frackowiak et al., 1995), which is limited, however, to field offsets whose spatial structure matches the distortion model used.

Higher-frequency fields that vary significantly during EPI readouts are almost exclusively driven by gradient operation, with potential contributions from active shimming when performed dynamically (Duerst et al., 2015; Sengupta et al., 2011; van Gelderen et al., 2007). Hardware trade-offs and imperfections give rise to a range of typical errors in these field components. Most prominent among these are the general low-pass behavior of gradient and shim chains, delays, eddy currents, mechanical vibrations, and gain drifts. In single-shot EPI they result in a variety of artifacts, most prominently in ghosting but also in blurring, shearing, and other distortion. When these mechanisms vary over time the related artifacts fluctuate in time series and again become confounds to fMRI. Gradient system imperfection is traditionally addressed by waveform pre-distortion (pre-emphasis) and, for EPI, by data correction based on calibration. The standard calibration approach is to perform additional EPI readouts without phase-encoding blips. Correction settings are then derived from the inconsistencies of the echo train, capturing reproducible imperfections of the frequency-encoding gradient. Such calibration can be performed on a per-scan basis as well as, to sense system changes during a scan, on a per-shot basis by adding calibration echoes at the beginning of each actual EPI readout (Bruder et al., 1992; Hinks et al., 2006; Schmitt et al., 1998).

Navigators and calibration echoes have in common that they rely on NMR signal from the head for field observations. Alternatively, field measurements can also be performed with external NMR sensors, which permit field recording concurrently with image readouts (Barmet et al., 2010, 2009, 2008; De Zanche et al., 2008; Wilm et al., 2011). With this approach, the evolution of B_0 and gradient fields can be captured without requiring additional time or reproducibility of field behavior. Unlike EPI calibration it does not rely on intrinsic repetitiveness of gradient waveforms, permitting field error correction also for, e.g., variable-density EPI and spiral scanning (Kasper et al., 2014; Vannesjo et al., 2016a).

The diversity of types and sources of field perturbations prompts the question which mechanisms dominate in fMRI time series and how large the associated confounds are. Given the different options for addressing field errors it is also important which spatial terms need to be accounted for and at which temporal resolution. A recent study targeted these questions for hardware-related perturbations, performing fMRI scans in a phantom with field monitoring by external sensors (Kasper et al., 2015). In this study relevant variability over time series was observed in both the uniform and gradient field components, exhibiting slow as well as within-shot dynamics. It resulted in image fluctuations ranging between 1% and 10%, depending on spatial order, yet permitted effective retrospective correction using field recordings.

Based on these findings, the goal of the present contribution is to establish how they translate to fMRI in vivo. Specifically, it aims to explore the structure and magnitude of additional field fluctuations of physiological origin, the severity of related image fluctuations, and whether field recording and retrospective correction are equally effective in the in vivo scenario.

2. Methods

Investigation of field fluctuations and their impact on standard fMRI was performed in vivo at 3 Tesla, using the following study design:

- Acquisition of 2D EPI time series in vivo with concurrent field monitoring.
- Extraction of prominent fluctuations of the background field and EPI trajectories using principal component analysis (PCA).
- Spectral separation of physiological field fluctuations from hardware-related perturbations.
- Analysis of image fluctuations caused by field fluctuations of different spatial order and origin.
- Isolation of field-mediated effects from other fluctuations, using simulation.
- Quantification of BOLD sensitivity gained by retrospective field correction.

2.1. Setup

We used the same hardware setup as described in the preceding phantom study (Kasper et al., 2015) to facilitate comparison between phantom and in vivo results. Image data was acquired on a Philips Achieva 3 T system, using an 8-channel head coil array. Field monitoring was performed with an array of 12 transmit/receive field probes (Barmet et al., 2009, 2008; De Zanche et al., 2008) based on ^{19}F NMR for operation concurrent with imaging readouts (Barmet et al., 2010; Wilm et al., 2011). The probe array was mounted on the inside of the head coil as illustrated in Wilm et al. (2015).

2.2. Subjects and imaging protocol

We carried out a total of 18 fMRI sessions, including four healthy subjects (BMI 19–25, two female) after written informed consent and with approval by the local ethics committee. All but one of the subjects underwent three sessions, successively on one day. One subject (subject 1) underwent the three-session protocol repeatedly on three days to examine within-subject variability.

Each session consisted of 405 scans of which the first 5 were excluded to ensure image acquisition in a steady state, yielding a duration of 20 min per session. The imaging sessions were interleaved with equally long physiological monitoring sessions (20 min) during which field monitoring continued but no imaging was performed. The physiology-only sessions served to study physiological fields in the absence of gradient operation and to include periods of hardware cool-down as typically occurs between sessions or during the arrival of a new subject. After the second imaging session, the participants left the scanner for a 20-min break. Thus, repositioning and reshimming were performed before the third imaging session.

All fMRI sessions used a 2D single-shot EPI sequence in oblique-transverse orientation with an AP tilt of −20°, with the following parameters: TR 3 s, TE 35 ms, EPI readout duration 41.6 ms, 24 Hz BW/pixel, fundamental frequency of the EPI readout waveform 1034 Hz, phase encoding direction anterior-posterior, receiver bandwidth 375 kHz, voxel size 2.6×2.6×2.5 mm^3, FOV 220×220×47.5 mm, 10 slices with 2.5 mm inter-slice gap. Except for the slight slice tilt the sequence parameters were chosen identical to those used in the phantom study to allow direct comparison. During fMRI the subjects performed a social learning experiment (Diaconescu et al., 2016; Diaconescu et al., 2014) to ensure typical experimental conditions. For the physiology-only sessions, subjects were instructed to keep still and relax. Throughout, the cardiac cycle and respiration were recorded using electrocardiography (ECG) and a breathing belt.

2.3. Concurrent field monitoring and image reconstruction

The signal phase time courses of the field probes were preprocessed as described in Barmet et al., (2008), and expanded into second-order spherical harmonics comprising a total of 9 spatial terms. The zeroth-order term, $k_0(t)$, reflects phase accrued due to global field, i.e. the spatially uniform B_0. The first-order terms, $\boldsymbol{k}(t)=(k_1(t),\ k_2(t),\ k_3(t))$, reflect phase accrual of first order in space according to the common k-space formalism. After rotation and translation into the 2D slice geometry, $k_p(t)$ and $k_m(t)$ represent the first-order components in the phase-encoding and measurement directions. They form the 2D EPI trajectory and are jointly referred to as $\boldsymbol{k_{mp}}(t)$ in the following.

Image reconstruction was accomplished in three steps. First, each receiver coil signal was demodulated by the global phase $k_0(t)$ and the first-order component orthogonal to the imaging slice, scaled by the slice offset. Second, per-coil reconstruction was performed by applying the Moore-Penrose inverse of the encoding matrix

$$E = \exp(i\boldsymbol{k_{mp}}(t_\tau)\cdot\boldsymbol{r}_\rho) \tag{1}$$

which has one row τ per sampling point in time and one column ρ per voxel location in the slice plane. Inversion and matrix-vector multiplication were carried out jointly using conjugate-gradient iteration (Pruessmann et al., 2001) with gridding operations for efficient non-Cartesian Fourier transform (Beatty et al., 2005; Jackson et al., 1991; Pruessmann et al., 2001). Third, a compound array image was obtained by root-sum-of-squares combination. Image reconstruction and processing were implemented in MATLAB (R2013a, The MathWorks, Inc., Natick, Massachusetts, United States).

2.4. Analysis of field fluctuations

2.4.1. Principal component analysis of phase coefficients

PCA (Pearson, 1901) of the phase coefficients $k_0(t)$, $k_m(t)$, and $k_p(t)$ was performed in the same way as described in the preceding study (Kasper et al., 2015). PCA determines subspaces that best capture the variance of the given data and was achieved by eigendecomposition of the covariance matrix

$$COV^l_{\tau,\tau'} = \frac{1}{N-1}\sum_{n=1}^{N}(k_{l,n}(t_\tau) - \overline{k}_l(t_\tau))\cdot(k_{l,n}(t_{\tau'}) - \overline{k}_l(t_{\tau'})), \tag{2}$$

where n is the scan number, $l = 0, m, p$, and the bar indicates the mean over all scans of one subject, i.e., N=9×400 or N=3×400, respectively.

The principal components (PC), given by the eigenvectors of the covariance matrix, are orthogonal and ranked by the magnitude of the associated eigenvalues, which reflect the amount of variance captured. Each PC represents a characteristic fluctuation around the mean time course of the respective phase coefficient. How much a given PC contributes at any given time is assessed by computing the projection of $k_l(t)$ onto that PC. Time series of PCA projections reflect variation in the presence of field fluctuation patterns over sessions, days and subjects.

2.4.2. Spectral separation of physiological and hardware-related field fluctuations

Separation of hardware-related and physiological field fluctuations was based on the frequency content of their PCA projections in conjunction with ECG and breathing belt recordings. First, we estimated the spectral density of the PCA projections by computing the discrete Fourier transform of the projections per session and averaging their amplitude spectra across sessions (Bartlett, 1948). Based on the physiological recordings we categorized projection content between 0.15 Hz and 1.2 Hz as physiological fluctuations. To select physiological projection contents, denoted by $proj_{Phys}$, we designed a corresponding Butterworth bandpass filter using the Signal Processing Toolbox in Matlab (The MathWorks, Inc., Natick, Massachusetts, United States), damping frequencies below 0.1 Hz and above 1.4 Hz by at least 15 dB.

The hardware-related content in each projection, $proj_{HW}$, was computed as the difference between the original projection and the physiological projection content. On this basis, phase coefficients containing only hardware-related fluctuations, $k_{l,\ HW}^{(n)}(t)$, were generated by subtracting the physiological projections times the corresponding principal components from the measured phase coefficients:

$$k_{l,\ HW}^{(n)}(t) = k_l^{(n)}(t) - \sum_{c=1}^{N_c}\left(proj_{c,l,Phys}^{(n)}\cdot PC_c(t)\right) \tag{3}$$

where c counts the principal components and N_c, the number of components included, which was chosen such as to capture at least 99% of variance in subject 1.

Similarly, phase coefficients containing only physiological field fluctuations, $k_{l,Phys}^{(n)}(t)$, were constructed:

$$k_{l,Phys}^{(n)}(t) = k_l^{(n)}(t) - \sum_{c=1}^{N_c}\left(\left(proj_{c,l,Orig}^{(n)} - proj_{c,l,Phys}^{(n)}\right)\cdot PC_c(t)\right) \tag{4}$$

2.5. Reconstruction schemes

Image reconstruction was performed repeatedly, varying the field monitoring information included (Table 1). Reconstruction using all concurrent field monitoring information throughout served as a reference. To investigate the impact of field fluctuations of different spatial order and origin we used a 2×2 factorial design of reconstruction schemes, in each of which knowledge of one type of fluctuations, k_0 or $\boldsymbol{k_{mp}}$ of physiological or hardware origin, was neglected. For example, to consider physiological fluctuations in k_0, the concurrently monitored phase coefficients of $\boldsymbol{k_{mp}}$ were used for reconstruction while the preceding demodulation was performed using only $k_{0,HW}$, i.e., the hardware-related part of k_0 fluctuations. In this way, encoding errors by physiological k_0 fluctuations were allowed to propagate into the image time series. For the three other types of fluctuation reconstruction schemes were created in an analogous manner (Table 1). To study the combined impact of all field fluctuations we employed a field-averaged scheme using the respective session mean of k_0 and $\boldsymbol{k_{mp}}$ for reconstruction. In this case all field fluctuations propagated into the image time series while stable field imperfections, such as reproducible eddy current effects, were corrected for, similarly to per-session EPI

Table 1
Reconstruction Schemes (n – index of scan within session, t – sampling time within readout, overbar – average over all scans of one session). Scheme #1 uses all field information available, schemes #2–#5 ignore the indicated type of field fluctuation. Scheme #6 ignores all field fluctuations.

	Reconstruction Schemes	Phase Coefficients Used	
		$\mathbf{k_0}$	$\mathbf{k_{mp}}$
1	Full Field Correction (Concurrent Monitoring)	$k_0^{(n)}(t)$	$k_{mp}^{(n)}(t)$
2	Hardware-related Fluctuations, k_0	$k_{0,Phys}^{(n)}(t)$	$k_{mp}^{(n)}(t)$
3	Hardware-related Fluctuations, k_{mp}	$k_0^{(n)}(t)$	$k_{mp,Phys}^{(n)}(t)$
4	Physiological Fluctuations, k_0	$k_{0,HW}^{(n)}(t)$	$k_{mp}^{(n)}(t)$
5	Physiological Fluctuations, k_{mp}	$k_0^{(n)}(t)$	$k_{mp,HW}^{(n)}(t)$
6	Field-Averaged	$\overline{k_0}(t)$	$\overline{k_{mp}}(t)$

calibration.

Reconstructed image time series were further processed in two forms, once unaltered and once after additional rigid-body image co-registration ("realignment") as an alternate means of addressing slow global field changes in EPI. Realignment was performed with SPM 12 (Wellcome Trust Centre for Neuroimaging, London, UK, http://www.fil.ion.ucl.ac.uk/spm/).

2.6. Simulations

To assess field-mediated image fluctuations separately from other mechanisms such as radiofrequency fluctuations and physiological noise we generated synthetic raw data afflicted by field fluctuation only. This was achieved by forward calculation of signal encoding with the concurrently measured phase coefficients k_0 and $\boldsymbol{k_{mp}}$ for all sessions performed with subject 1. The underlying numerical phantom was created from the data of session 1 by reconstruction on the basis of concurrent monitoring, averaging over time, and removal of background noise and non-brain tissue. Image reconstruction from the synthetic data followed the same schemes as described earlier (see Table 1).

2.7. Statistical analysis of image fluctuations

We studied the impact of field fluctuations on BOLD sensitivity by calculating the voxel-wise signal-to-fluctuation-noise ratio (SFNR) (Welvaert and Rosseel, 2013) resulting from the different reconstruction schemes as

$$SFNR(\boldsymbol{r_\rho}) = \frac{\overline{img(\boldsymbol{r_\rho})}}{SD(img(\boldsymbol{r_\rho}))} \tag{5}$$

where the mean and the standard deviation (SD) of each image intensity value $img(\boldsymbol{r_\rho})$ are taken over the N=390 scans of a session (omitting the first and last 5 scans for lead-in and -out of the filters that separate physiological and hardware-related components). Since the same data entered all reconstruction schemes, SFNR differences purely reflect effects of field fluctuations and their correction.

SFNR gains associated with correction of field fluctuations were quantified by comparing reconstruction schemes #2–#6 with the reference scheme #1 in terms of average SFNR. For example, the relative SFNR gain when correcting physiological fluctuation in k_0 reads

$$\Delta SFNR = \frac{\langle SFNR_{Concurrent\ Monitoring}\rangle - \langle SFNR_{k_0,Phys}\rangle}{\langle SFNR_{k_0,Phys}\rangle}\cdot 100 \quad \%, \tag{6}$$

where the brackets indicate averaging over all voxels in a given region of interest (ROI). Five ROIs were defined based on the tissue-segmented (Ashburner and Friston, 2005) mean image: whole-brain gray matter, frontal gray matter, occipital gray matter, white matter, and gray/white matter boundaries to study the impact of small displacements.

In occipital gray matter, SFNR gains were also studied on a per-voxel basis. For this purpose we slightly smoothed the underlying SFNR maps (Gaussian kernel, $FWHM = 1.5\cdot voxel\ size$) to account for subtle geometric differences due to different levels of field correction.

To investigate possible differences in SFNR gains across sessions, we estimated the correlation coefficient for mean SFNR gain and the SD of heart rate and respiration across sessions. To assess the impact of movement, we correlated the mean SFNR gain with the SD of the realignment parameters for translation and rotation.

3. Results

3.1. Characterization of field fluctuations

This section reports the field fluctuations observed with subject 1 who performed the experiment repeatedly on three different days. The field recordings obtained with the other subjects were similar, both qualitatively and quantitatively, particularly the dominant features of the principal components, the amounts of explained variance (99 ± 2%), and the temporal evolution of PCA projections.

For all phase coefficients, 99% or more of the variance across scans was explained by at most two principal components (Fig. 1, left column). For k_0, the first principal component (PC 1) explained 99.996% of the variance over all 9 sessions. For k_p, PC 1 explained 99.7%. For k_m, i.e., first-order phase in the readout direction, the first and second principal components explained 94.2% and 4.6% of the variance.

Each of the found PCs exhibits a subset of three distinct features: (i) a linear increment, (ii) an oscillating component at the fundamental frequency of the EPI readout of approximately 1 kHz, and (iii) amplitude modulation of that oscillation at about 10 Hz. The linear increment, which occurs in the first PC of each spatial term, corresponds to a field that is static on the time scale of the EPI readout and thus reflects a slow field change. The oscillation at the EPI frequency is present in all PCs of the gradient fields and the modulation at 10 Hz was found in both PCs of the gradient in the measurement direction, k_m. Notably, these PC features correspond closely to those found in the previous phantom study (Kasper et al., 2015), in which the 10-Hz modulation was attributed to thermal change in mechanical resonance behavior. The PCs of the sessions without image acquisition exhibited linear increments as well, but no oscillations. This indicates that field fluctuations of physiological origin are slow on the time scale of the EPI readouts and that the presence of the subject does not significantly alter gradient and magnet behavior.

The projections of the PCs (Fig. 1, central column) show the change in amplitude of these typical fluctuation patterns over sessions and days. The within-session dynamics were broadly reproducible between sessions and days, apart from offsets reflecting varying initial conditions such as system temperature and shim settings. For the PCs dominated by linear increments the projections reflect the respective slope and thus the magnitude of the underlying field change. A projection change of 1 unit translates into a field change of approximately 4 Hz (1rad/41.6ms≈24/2π Hz). Hence the observed projection changes represent field fluctuations of 31 Hz in k_0, 50 Hz/m in k_p and 15 Hz/m in k_m within session.

The projection dynamics exhibit three main features within-session: approximately linear drifts, saturating drifts akin to exponential behavior, and faster periodic oscillations with a 4–5 s cycle length (≈0.25 Hz) (Fig. 1, right column). Linear drift dominates the projection of PC 1 in k_0 and k_m. It is continuous between sessions 1 and 2 of each day but starts with an offset in session 3 due to repositioning and reshimming. The saturating drift is prevalent in the projections of

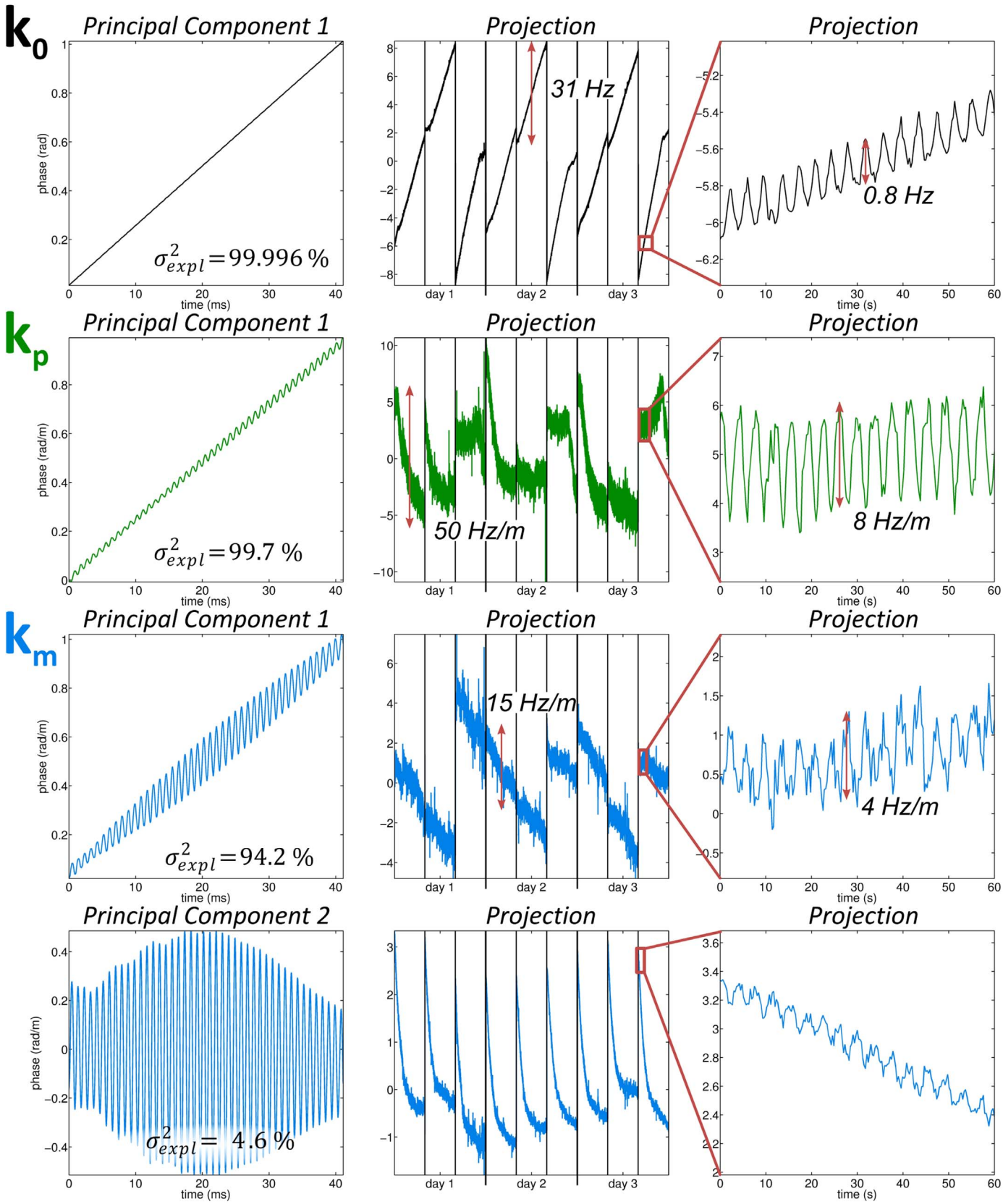

Fig. 1. Principal Component Analysis (PCA) of field fluctuations of subject 1 (9 sessions on 3 different days). (Left) First principal component (PC) for global phase (k_0) and phase-encoding (k_p) phase coefficients. First and second PC for frequency-encoding (k_m) phase coefficient. Most PCs exhibit a linear drift (k_0, k_m, k_p) and oscillation at the fundamental EPI readout frequency (k_m, k_p). (Center) Corresponding projections on the PCs. (Right) Zoomed projections. A periodic oscillation (4–5 s cycle) is visible in all PCA projections. Based on comparison with breathing-belt recordings it is attributed to breathing (see also Fig. 2).

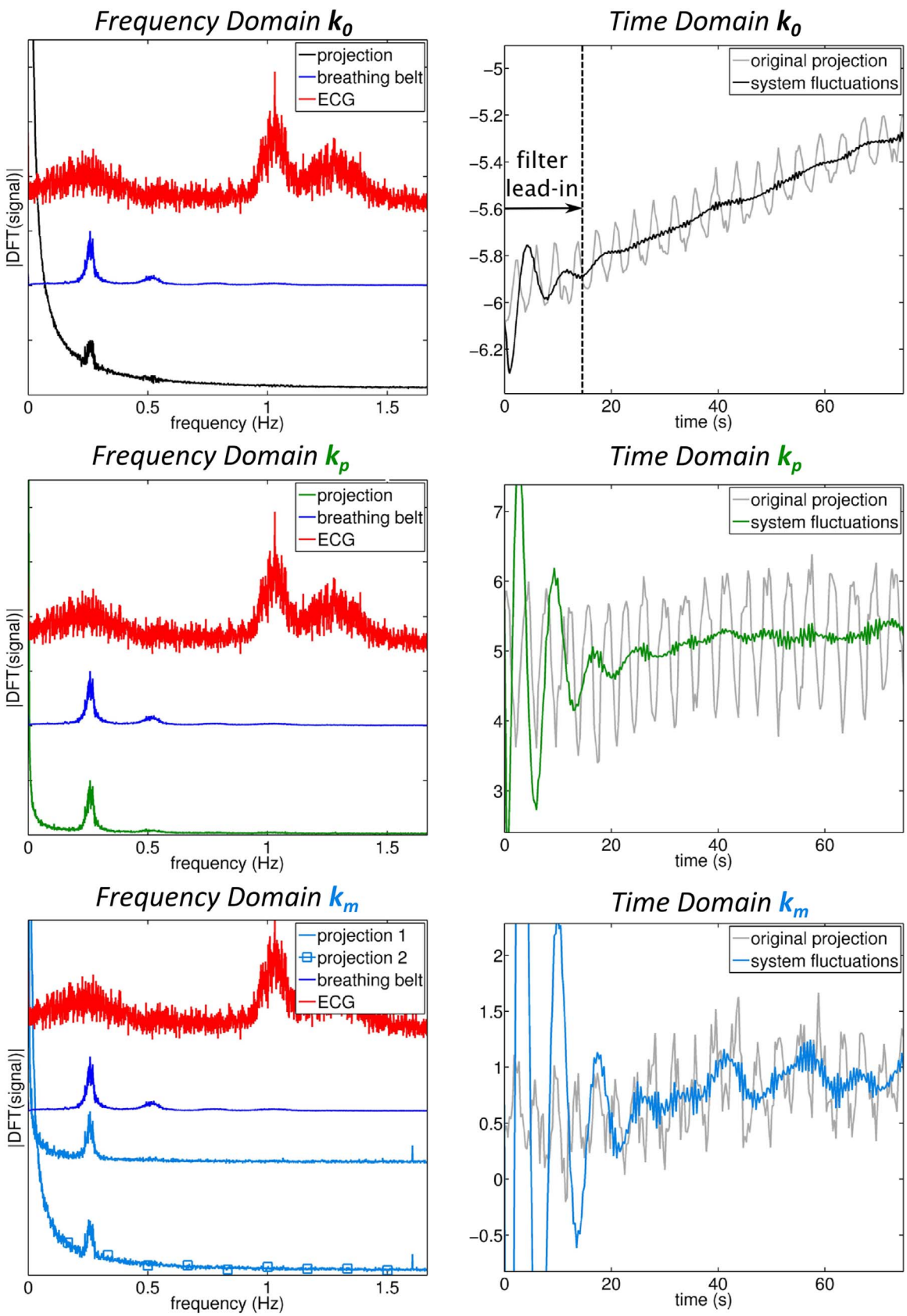

Fig. 2. Disentangling physiological and hardware-related field fluctuations in the PCA projections. (Left) Amplitude spectrum of the projections of PC 1 for k_0 and k_p and PC 1 and PC 2 for k_m, compared with breathing-belt and ECG recordings. All projections share the distinct breathing peak at about 0.25 Hz. (Right) Remaining fluctuations in the PCA projections after removal of the physiological frequencies, reflecting hardware-related fluctuations. The unchanged projections are depicted in gray for comparison, and the lead-in time of the filter is indicated.

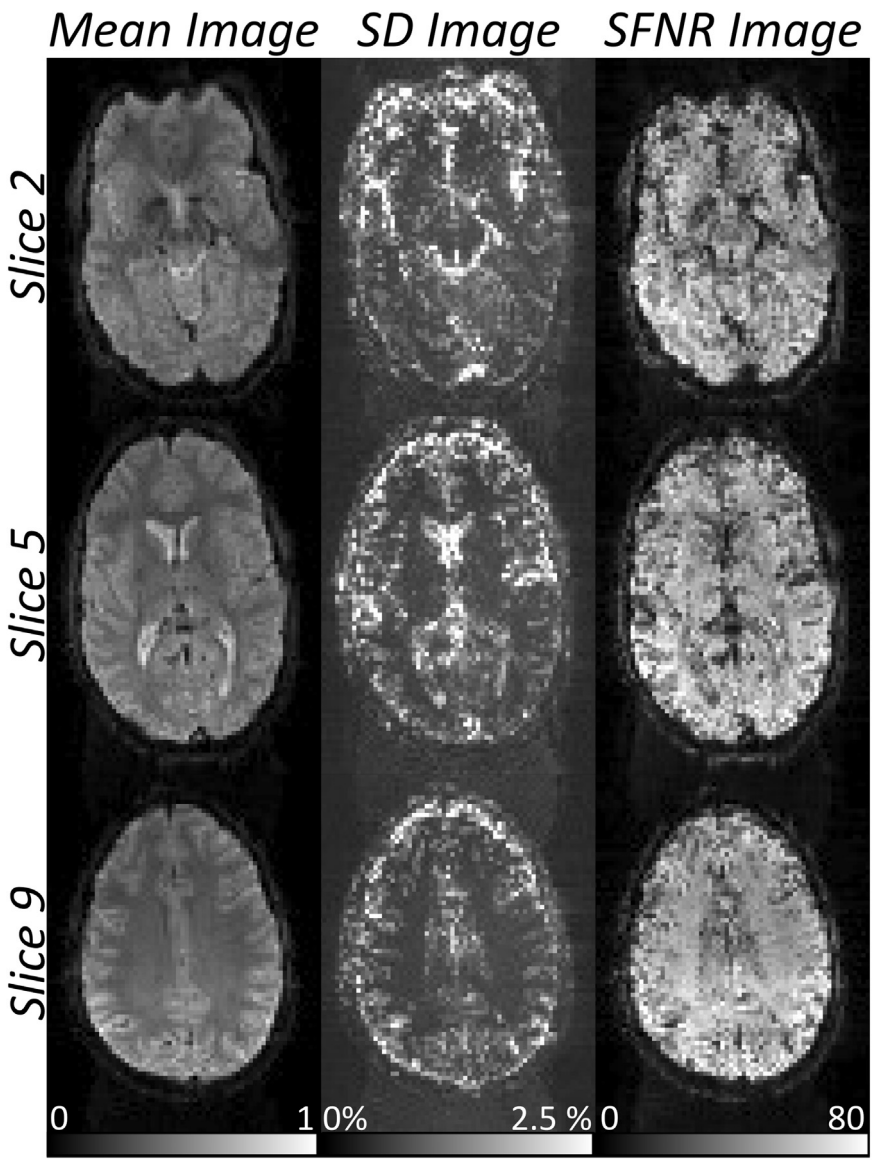

Fig. 3. Summary statistics after realignment of EPI session 1, day 1, subject 1, reconstructed with full field correction. (Left) Mean images over 390 scans of an inferior, central and superior slice (top to bottom). (Center) Voxel-wise standard deviation (SD) of the same session (scaling in percent maximum intensity of the mean image). (Right) Signal-to-fluctuation-noise ratio (SFNR), ratio of corresponding mean and SD images.

PC 1 for k_p and PC 2 for k_m. Oscillation at about 0.25 Hz is present in all projections of k_0, k_p and k_m (Fig. 1, right column), reaching amplitudes of 2.5%, 15% and 25% of the respective projection range for the dominant first PCs, corresponding to field fluctuations of 0.8 Hz, 8 Hz/m and 4 Hz/m, respectively.

Similar global features of linear and saturating drifts were found in the preceding phantom study (Kasper et al., 2015), indicating their origin in the instrumentation used. Oscillations at frequencies on the order of 0.25 Hz were absent in the phantom experiment but prominent in the physiology-only monitoring sessions in the present work (see Supplementary figure S1). They are thus of physiological origin and, based on their frequency, apparently caused by breathing. This is confirmed by comparing the spectra of the projections (Fig. 2, left column) with those of the conventional physiology recordings. The peak at 0.25 Hz and a first harmonic are shared with the breathing belt spectrum. In contrast, no trace of the ECG spectrum is apparent in any of the PCA projections. The right-hand column Fig. 2 illustrates band-pass filtering of the PCA projections to separate physiological and hardware-related fluctuations as described in Section 2.4.2.

3.2. Image reconstruction with full field correction

We present the session statistics (mean, SD, SFNR) of one realigned EPI time series (subject 1/day 1/session 1) reconstructed with full field correction (scheme #1), which were representative for all sessions and subjects. The mean images exhibited no visible ghosting or blurring independent of the slice position (Fig. 3, left). Static B_0 inhomogeneity caused common distortions and mild dropouts in inferior slices. The SD images (Fig. 3, center) reveal fluctuations below 2.5% of maximum image intensity for the majority of voxels, with highest values in CSF-bearing regions, particularly in the ventricles and the subarachnoid space. Slight N/2 ghosting is discernible here, reflecting ghosting that fluctuates over time, and an SD increase in frontal regions of the inferior slice, i.e., in the presence of B_0 inhomogeneity. The SFNR images (Fig. 3, right) show rather uniform SFNR across the imaging volume, with significant drops only in CSF, inferior-frontal and medial regions, at a mean SFNR of about 50 in the brain.

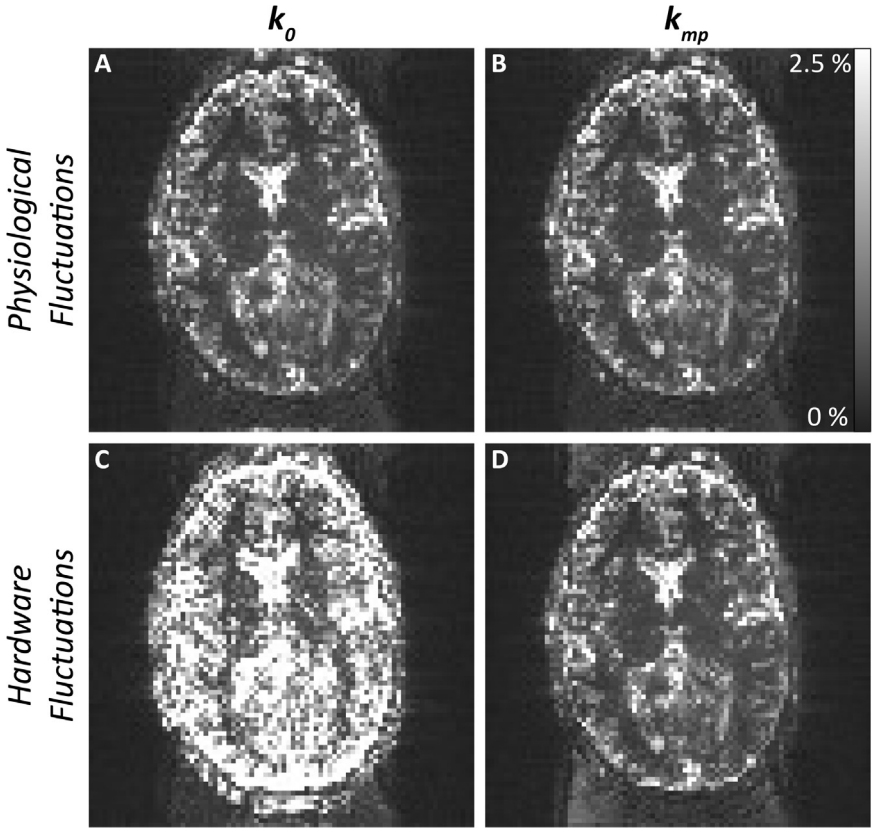

Fig. 4. SD images of measured EPI time series (subject 1, day 1, session 1) resulting from different reconstruction schemes (equal scaling, in percent maximum intensity of the mean image). (A, B) Physiological fluctuations in k_0 and $\boldsymbol{k_{mp}}$ do not induce discernible alterations of the SD distribution relative to full field correction (Fig. 3). (C) Hardware-related fluctuations in k_0 increase SD values, primarily at tissue boundaries. (D) Hardware-related fluctuations in $\boldsymbol{k_{mp}}$ increase the SD via the fluctuating ghosting artifact.

3.3. Characterization of field-induced image fluctuations

To study the impact of different field fluctuations on image fluctuations, we compared SD images of the reference reconstruction (Fig. 3) with SD images of reconstructions with only partial field correction (Table 1). Given the observed similarity of session statistics between slices, we focus on a central slice (5) in the following.

When omitting correction for physiological field fluctuations no difference to the reference SD map is visible in the measured data (Fig. 4AB). The effects of physiological field fluctuation are thus subtle and masked by other confounds, such as BOLD fluctuations and CSF dynamics. The magnitude of the physiological field effects is evident, however, from corresponding SD maps generated from the simulated data with all but field fluctuations suppressed. As shown in Fig. 5AB, they are on the order of 0.2% (k_0) and 0.1% ($\boldsymbol{k_{mp}}$) maximum image intensity. Fluctuations in k_0, causing jittering image shifts, are manifested in enhanced SD at tissue boundaries (Fig. 5AC). The physiological fluctuations in $\boldsymbol{k_{mp}}$ give rise to similar effects, yet of increasing magnitude towards the periphery in the phase encoding direction, which reflects jittering image scaling in that dimension (Fig. 5B).

Omitting correction for hardware-related field fluctuations (Fig. 4CD) the SD increases strongly for k_0 fluctuations (Fig. 4C) and moderately due to $\boldsymbol{k_{mp}}$ fluctuations (Fig. 4D). The complementary analysis based on simulation revealed field-related SD on the order of 5% due to k_0 fluctuations, again predominantly at tissue boundaries (Fig. 5C). First-order fluctuations ($\boldsymbol{k_{mp}}$) caused SD up to 0.6%, most prominently in the form of delay-type N/2 ghosting yet also at tissue boundaries due to jitter of scaling in the phase-encoding direction (Fig. 5D).

3.4. Impact of field correction on SFNR

The relative impact of different field fluctuations on SFNR followed their ranking in SD contributions, with higher SFNR gains when correcting for hardware-related compared to physiological fluctuations, and for k_0 compared to $\boldsymbol{k_{mp}}$ (Fig. 6, Table 2, Fig. S2). For example, correcting for hardware-related k_0 fluctuations in gray matter resulted in 66.7% SFNR gain and thus afforded nearly all of the 70.1% gain of full field compared to field-averaged correction.

However, SFNR gains within ROIs varied considerably (Fig. 6, each boxplot representing distribution over voxels). For example, SFNR gain correcting for physiological fluctuations in k_0 was small on average (0.4%), but exceeded 1% in a quarter of the occipital gray matter voxels for subject 1 (Fig. 6, top left).

Moreover, SFNR gains exhibited intra- and inter-subject variability (Fig. 6, 1 boxplot per session, 1 color range per subject), and more so for $\boldsymbol{k_{mp}}$ than k_0. Non-field sources of physiological noise, i.e., subject motion and, to a lesser degree, cardiac and respiratory characteristics, contributed to this variability. Mean SFNR gain, taken over all sessions and reconstruction schemes, correlated negatively with SD of realignment parameters (translation −0.62, rotation −0.67), heart rate (HR, −0.36) and respiratory volume per time (RVT, −0.27). However, intrinsic correlation between motion and HR (0.50) or motion and RVT (0.37) precluded a unique attribution of their impact.

We further studied the effect of realignment on SD images and SFNR for the full field reconstruction and the field-averaged reconstruction (Fig. 7, see also Fig. 6 vs S2 for other reconstruction schemes). Before realignment, the fluctuation levels in the SD images were much higher in the field-averaged reconstruction compared to full field correction (Fig. 7A), in particular at tissue boundaries, indicative of shifts. Consequently, very marked differences in SFNR between field-averaged reconstruction and full field correction were apparent in all sessions and subjects, with a median SFNR improvement between 40% (white matter) and 105% (occipital gray matter) (Fig. 7B, top, boxplots representing distribution over 18 sessions).

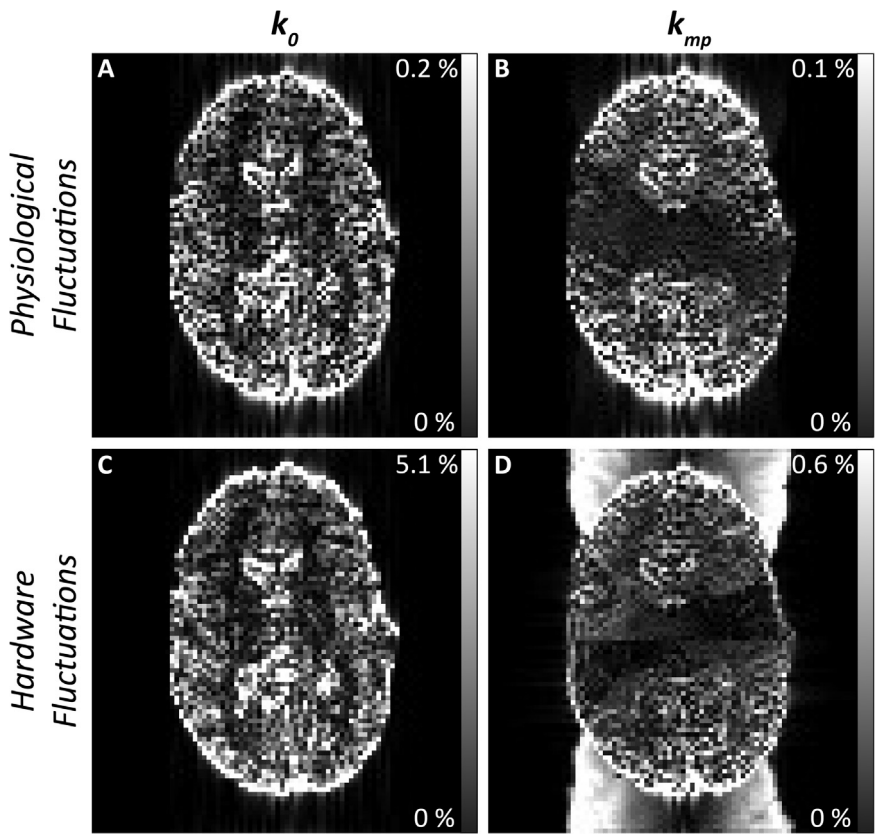

Fig. 5. SD of reconstructions from simulated data perturbed by measured field fluctuations only (scaling in percent maximum intensity of the mean image). (A) Physiological fluctuations in k_0 cause SD up to 0.2%, by jittering image shifts. (B) Physiological fluctuations in $\boldsymbol{k_{mp}}$ cause SD up to 0.1% by jittering image scaling. (C) Hardware-related k_0 fluctuations cause SD up to 5% by image shifts. (D) Hardware-related $\boldsymbol{k_{mp}}$ fluctuations cause N/2 ghosting and image scaling effects, with SD up to 0.6%.

After realignment, SD levels in the field-averaged reconstruction were considerably reduced, while SD in full field correction appeared unaffected by realignment. Overall, a moderate SFNR gain prevailed when using full field correction, pronounced in occipital gray matter (5–15%, median 12%) and N/2 ghosting sites, but negligible in white matter.

4. Discussion

4.1. Field fluctuations in in vivo EPI time series

The reported experiments confirm that field fluctuations of physiological origin are present in the head during fMRI studies. Breathing was identified as the cause of field perturbations of both 0th and 1st order in space. The perturbing fields were found to be on the order of 1 Hz and 10 Hz/m, respectively, at the employed field strength of 3 T. In single-shot EPI time series such perturbations cause jittering shifts and scaling of reconstructed images. With typical sequence parameters these jitters gave rise to subtle fluctuation of brain image intensities on the order of per mills of the maximum signal value. The related impact on the SFNR was small in the presence of larger image fluctuations of different origin. Field fluctuations of cardiovascular origin and related image fluctuations were not observed. Magnetic fields due to susceptibility effects of the beating heart have previously been recorded (Gross et al., 2016; Pruessmann et al., 2011), however closer to the heart and at higher field (7 T). The present study suggests that at 3 T long-range fields of cardiovascular origin can likely be neglected in the head while those caused by breathing are present and do influence fMRI.

Field fluctuations of hardware origin were found to closely match the findings of the preceding phantom study. This indicates that the presence of a subject does not significantly alter drifts and other dynamics of magnetic field emanating from the magnet, gradients, and other parts of the instrumentation, as may be expected. Hardware-related field fluctuations were present in both 0th and 1st spatial order at magnitudes up to 31 Hz and 50 Hz/m, respectively. PCA and PCA projections revealed slow fluctuations that were virtually static over EPI readouts as well as recurring fast components whose amplitude varied along EPI series.

These findings are in line with studies conducted by other researchers and on different MR systems. Breathing-related field fluctuations of about 1 Hz in amplitude have previously been reported for 3 T (Henry et al., 1999) and proportionally larger effects (2–5 Hz) have been observed at 7 T (Duerst et al., 2015, 2016; Pfeuffer et al., 2002; Van de Moortele et al., 2002). Main field drifts of 1–3 Hz/min due to heating were found in fMRI and diffusion studies using 3 T and 7 T systems from different vendors (Alhamud et al., 2016; Duerst et al., 2015; Henry et al., 1999; Liu et al., 2001). Cool-down after SSFP sequences led to thermal drift on the same order of magnitude in a multi-center comparison (El-Sharkawy et al., 2006). Thermal modulation of ghosting in EPI, caused by changes in the mechanical behavior of gradient tubes, was previously observed in (Giannelli et al., 2010). In Foerster et al., (2005), mechanical resonances were additionally shown to influence the rate of main field drift. Change in the main magnetic field over long periods of time was assessed at 135 Hz/year in one study (Friedman and Glover, 2006).

4.2. SFNR impact of field fluctuations in vivo

4.2.1. Hardware-related field fluctuations

The impact of field fluctuations on image time-series varied between different spatial terms and origins (Figs. 6 and S2, Table 2). Hardware-related fluctuations dominated over their physiological counterparts, and k_0 over $\boldsymbol{k_{mp}}$. The largest effect was that of hardware-related fluctuation in k_0, resulting in a mean SFNR gain of 67%

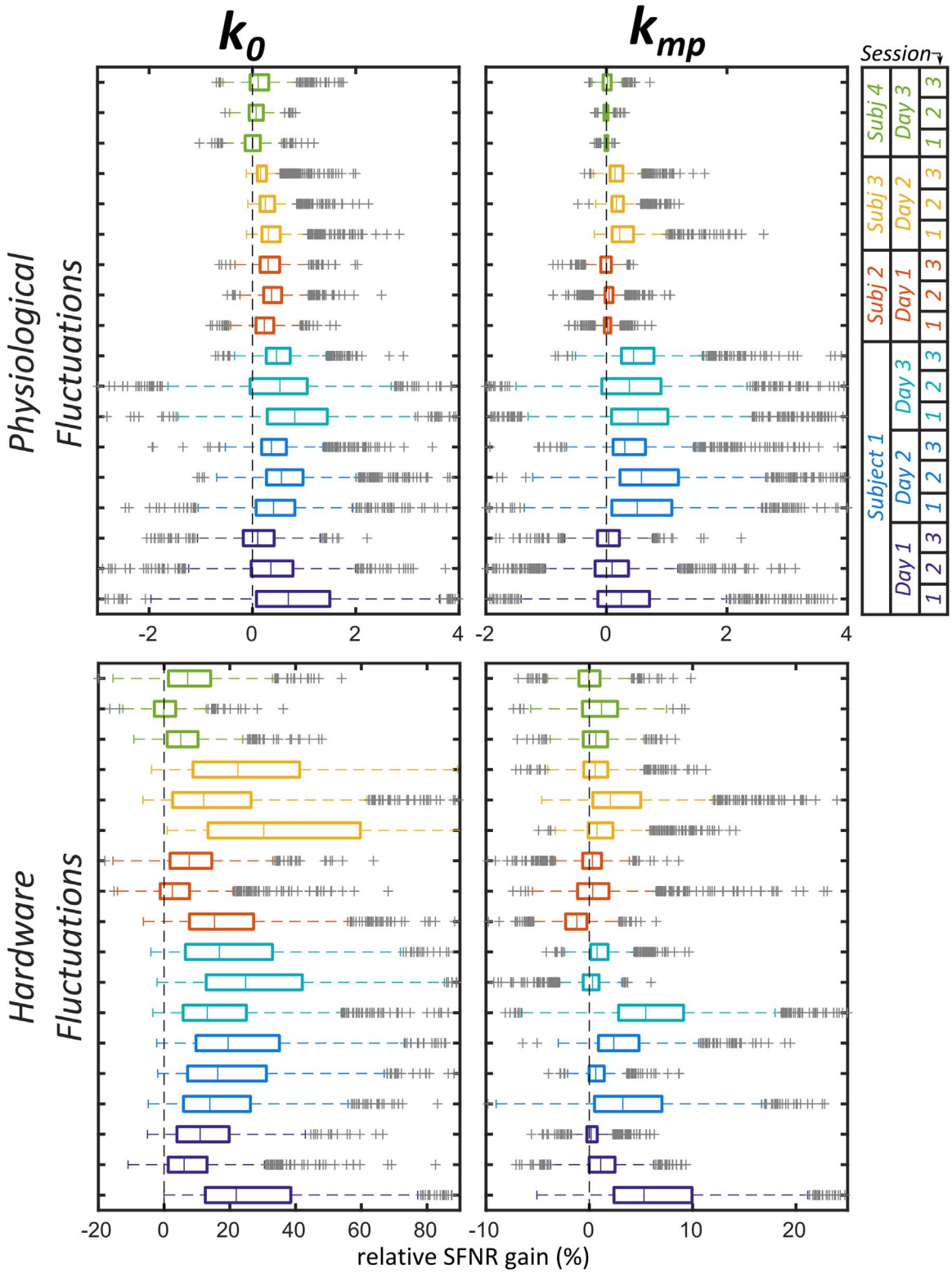

Fig. 6. SFNR gain in occipital gray matter per session for all subjects after realignment. Boxplots illustrate the distribution of SFNR gain over voxels within ROI (vertical line=median; box=25/75 percentile; whisker=up to one and a half times the interquantile range from the box; plus=outliers). The SFNR difference is taken with respect to the full field correction, and scaled relative to the SFNR in the respective reconstruction scheme. Correcting for physiological fluctuations in k_0 or $\boldsymbol{k_{mp}}$ results in a moderate SFNR gain of 1–2%. Correcting for hardware fluctuations yields higher SFNR gains of up to 40% in k_0, and up to 3% in $\boldsymbol{k_{mp}}$.

upon correction (in gray matter regions, before realignment). Correction of hardware-related fluctuations in $\boldsymbol{k_{mp}}$ resulted in only minor SFNR gain on the order of 1%. Relative to the previous phantom study, the impact of hardware-related fluctuations on the SFNR was comparable for k_0 and slightly reduced for $\boldsymbol{k_{mp}}$.

Realignment corrected for a significant part of the image fluctuations induced by k_0 fluctuations due to their manifestation as image shifts in EPI (Table 2). However, a relevant fraction of the SFNR loss was not recovered by realignment. Full field correction further increased the SFNR by 6% on average in cortical gray matter.

Table 2
SFNR gains by full field correction compared to different reconstruction schemes with partial correction. Mean SFNR evaluated in 5 different ROIs (A) without and (B) after image realignment. For each ROI-averaged SFNR gain, the mean ± standard deviation are reported over all 18 sessions and subjects. Highest SFNR gain is found for field-averaged reconstruction and hardware-related fluctuations in k_0 with and without realignment. SFNR gain in gray matter is higher than in white matter; values for gray/white matter border are in between.

(A) SFNR Gains by Full Field Correction *without* image realignment

	Hardware		*Physiological*		*Field-Averaged*
	k_0	k_{mp}	k_0	k_{mp}	k_0 & k_{mp}
Gray Matter	66.7 ± 16.0%	0.9 ± 1.1%	0.3 ± 0.2%	0.1 ± 0.1%	70.1 ± 17.2%
White Matter	38.5 ± 10.3%	0.6 ± 0.5%	0.2 ± 0.1%	0.0 ± 0.0%	41.5 ± 10.7%
Gray/White Matter - Border	56.5 ± 13.1%	0.7 ± 0.6%	0.3 ± 0.2%	0.1 ± 0.1%	59.4 ± 14.1%
Frontal Lobe Gray Matter	51.8 ± 11.6%	0.4 ± 1.4%	0.2 ± 0.1%	0.0 ± 0.1%	53.5 ± 13.4%
Occipital Lobe Gray Matter	111.8 ± 40.6%	2.5 ± 3.2%	0.4 ± 0.3%	0.3 ± 0.3%	112.5 ± 33.9%

(B) SFNR Gains by Full Field Correction *after* image realignment

	Hardware		*Physiological*		*Field-Averaged*
	k_0	k_{mp}	k_0 & k_{mp}	k_{mp}	k_0 & k_{mp}
Gray Matter	7.2 ± 4.5%	0.9 ± 1.2%	0.3 ± 0.2%	0.1 ± 0.1%	6.0 ± 3.9%
White Matter	1.7 ± 2.2%	0.6 ± 0.6%	0.2 ± 0.1%	0.0 ± 0.0%	0.7 ± 2.3%
Gray/White Matter - Border	3.8 ± 3.0%	0.8 ± 0.8%	0.3 ± 0.2%	0.1 ± 0.1%	2.7 ± 2.7%
Frontal Lobe Gray Matter	8.0 ± 5.4%	0.8 ± 1.0%	0.3 ± 0.1%	−0.1 ± 0.1%	7.0 ± 4.6%
Occipital Lobe Gray Matter	15.7 ± 9.3%	1.6 ± 2.2%	0.4 ± 0.3%	0.3 ± 0.3%	12.3 ± 7.5%

4.2.2. Physiological field fluctuations

SFNR gains from correction for physiological field fluctuations were small at well below 1% on average in gray matter regions, reaching voxel-wise peak values up to 4% (Fig. 6). This finding reflects the presence of dominant other causes of image fluctuations and contrasts with previous reports of physiological field effects causing up to 67% increase in time series standard deviation (Pfeuffer et al., 2002). Our results are rather in line with previous observations at 3 T (Windischberger et al., 2002). A minor part of the discrepancy to 7 T studies may be attributed to the scaling of susceptibility effects with B_0 (Van de Moortele et al., 2002). The magnitude of breathing effects also depends significantly on the physique of the subject and on breathing patterns (Duerst et al., 2015; Van de Moortele et al., 2002). Interaction has also been reported between slice orientation and distance to moving tissue (Van de Moortele et al., 2002). Along these dimensions, the position of our transverse oblique imaging slab centered close to the anterior commissure seems to be an intermediate parameter choice.

4.2.3. Co-factors and other sources of fluctuations

The relative impact of different noise sources on the SFNR in vivo depends strongly on the ROI. Signal variation due to field-induced voxel shifts is pronounced in ROIs comprising tissue edges (Pfeuffer et al., 2002). Basic detection sensitivity depends on the distance from the detector array and intrinsic signal fluctuation is elevated by pulsation near vessels or ventricles. As a consequence, field correction benefited the SFNR less in frontal compared to occipital areas, which differ in distance from the detector, and in CSF. In addition, we observed strong correlation between head motion and SFNR gain by field correction, which reflects a sustained need for motion correction. This marks an important difference from the preceding phantom study, in which field-induced image fluctuations dominated throughout.

In the head we observed no magnetic fields of cardiovascular origin and only small respiratory fields of limited impact on the SFNR (0.2%). However, physiological noise correction based on peripheral recordings (Glover et al., 2000; Salimi-Khorshidi et al., 2014) consistently improves the SFNR in the high percent range (Murphy et al., 2013). Hence, the majority of breathing and cardiovascular image dynamics must be mediated by physics other than long-range magnetic field such as vessel pulsation, bulk motion, and the magnetic susceptibility of blood. The spatial structure of physiological noise also differs greatly from field-related noise. For the data considered here this is illustrated by RETROICOR correction (Glover et al., 2000; Harvey et al., 2008; Kasper et al., 2017) in Fig. S3 (Supplementary material). RETROICOR yielded essentially the same spatial structure and magnitude of SFNR gains with and without field correction, reflecting the small relative amplitude of the long-range field effects.

4.3. Implications for the correction of field fluctuations

In this work, field observations were performed with external NMR probes to capture fluctuations concurrently with actual EPI readouts and at full temporal resolution. This recent approach, combined with image reconstruction based on the field recordings, proved readily feasible in vivo and offered flexibility in studying different spatial field terms and time scales.

In current fMRI practice, field correction is performed by a choice of established methods as surveyed in the introduction, which shall be briefly reviewed in light of the findings of this work. Physiological fluctuations, occurring in all spatial terms, yet slow relative to EPI readouts, can be addressed by all of the established means, i.e. by calibration echo trains, navigators, and co-registration. For the latter, however, breathing fluctuations pose challenges. The length of breathing cycles is on the same scale as typical volume repetition times. Therefore co-registration of whole 3D stacks, as commonly done today, will not eliminate the breathing confounds. Moreover, jittering image scaling as observed in this work is not covered by rigid-body co-registration. To address breathing field effects co-registration should thus be performed on a per-slice basis and with at least an affine distortion model.

Of the established approaches only calibration echo trains permit accounting for within-shot field dynamics, as induced by hardware imperfections. To address fluctuations in these dynamics the calibration must be performed on a per-scan basis. This is straightforward in terms of sequence design and has no hardware implications. However, per-scan re-calibration requires a palpable acquisition time overhead and calibration echoes without phase encoding capture only repeated imperfections of the frequency-encoding gradient. They miss phase-

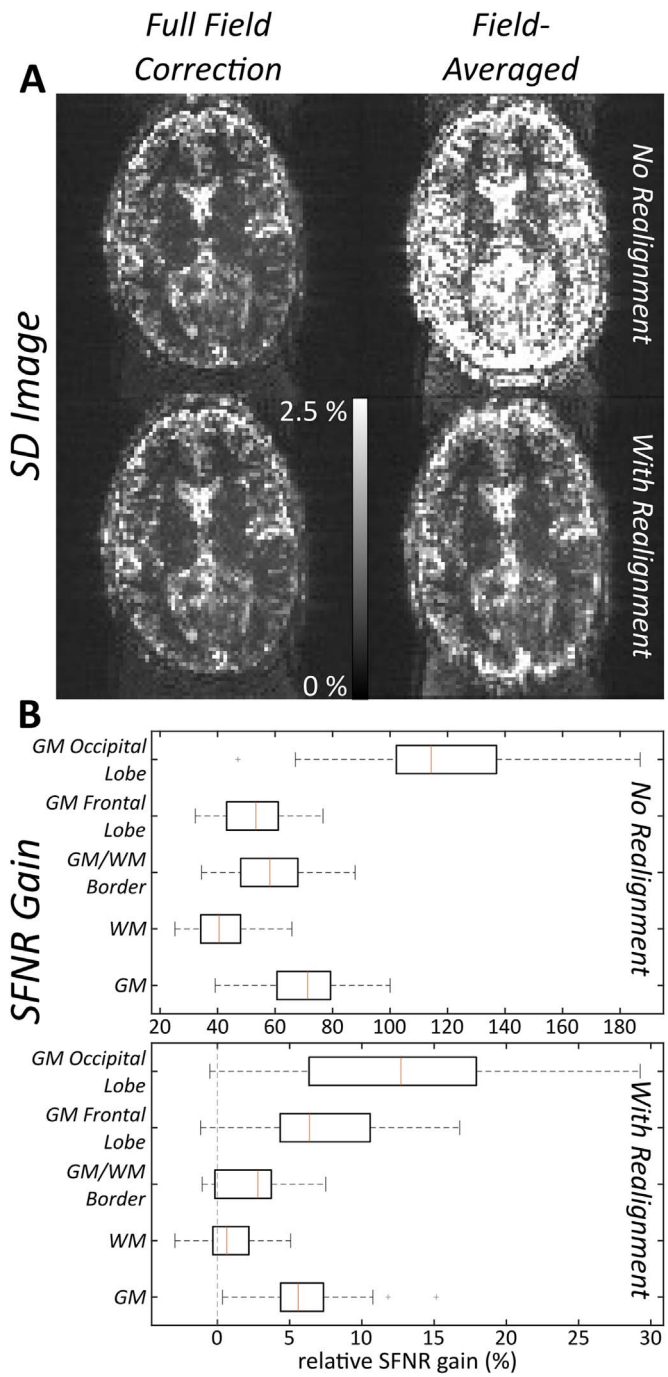

Fig. 7. Comparing full field correction to field-averaged image reconstruction (employing only the averaged field evolution over the session) for session 1, day 1, subject 1. (A) SD images before (top) and after (bottom) realignment. (B) SFNR gain for full field compared to field-averaged correction in different ROIs before (top) and after (bottom) realignment. The distribution (over sessions and subjects) of the mean SFNR gain is depicted (vertical line=median; box=25/75 percentile; whisker=up to one and a half times the interquantile range from the box; plus=outliers).

encoding errors and transient superposition behavior of all but very short-lived eddy currents.

In comparison, the key drawback of field monitoring with external probes is the need for additional instrumentation. Its chief advantage is coverage of all spatial field terms simultaneously, at full temporal resolution, and without sequence overhead. In addition, unlike calibration echoes concurrent field recording does not require that effects of interest occur repetitively and is thus equally applicable for other readout strategies such as spirals (Glover, 2012) and variable-density EPI (Kasper et al., 2014). Limitations of the signal lifetime of NMR field probes can be overcome by a continuous implementation using rapid re-excitation of short-lived sensor samples (Dietrich et al., 2016).

While the present work has been limited to field considerations up to 1st order in space, higher-order field perturbations can also be significant, particularly due to breathing (Vannesjo et al., 2015), eddy currents (Wilm et al., 2011), or dynamic shimming (Vannesjo et al., 2014). Measurement of higher-order field fluctuations is readily accomplished with navigators (Splitthoff and Zaitsev, 2009) and, for full temporal resolution, NMR field probes. However, image reconstruction with higher-order field correction involves substantially more computation than 1st-order reconstruction (Wilm et al., 2011) and will thus be challenging for fMRI time series.

A remaining fundamental limitation of data correction based on field observations is the requirement that data alterations caused by field perturbation be mathematically reversible. In single-shot scanning with small field perturbations this is true to a large degree but not without exception. In particular, slight slice displacement by field offsets during excitation cannot be addressed retrospectively. At typical excitation bandwidths of few kHz and field offsets as observed here, signal changes due to slice shift may well reach the percent range. A generic response to this issue is real-time rather than retrospective field correction, using suitable sensing and immediate actuation of compensation fields (Duerst et al., 2015; van Gelderen et al., 2007).

4.4. Translation to other fMRI scenarios

Field fluctuations and their translation into image fluctuations depend strongly on a range of sequence aspects, particularly the readout trajectory and associated artifact behavior, the gradient duty cycle, and potential parallel imaging acceleration. They also vary naturally with the hardware and correction strategies used as well as subject-related factors. Thus, the specific field behavior and image fluctuations observed in this work cannot be generalized. Instead the findings are intended to offer guidance regarding the types of effects encountered in typical fMRI studies at 3 T and, roughly, their orders of magnitude.

Beyond the common scenario studied here several directions of development are of particular interest in the context of field fluctuations. One of these is the gradual adoption of higher field strengths of 7 T and beyond for fMRI. Increasing B_0 boosts physiological field fluctuations by increasing the underlying susceptibility effects. FMRI at ever higher field will thus increasingly suffer from related image fluctuations. In addition to enhanced breathing effects low-order field perturbations of cardiovascular origin may eventually become a relevant confound. On the instrumentation side, stronger susceptibility effects have prompted efforts to deploy dynamic shimming at high field (Juchem et al., 2010, Vannesjo et al., 2016b), which will likely be a source of added hardware-related fluctuations.

A second intriguing direction is broader deployment of readout strategies other than regular EPI. One long-standing, attractive alternative is the use of spiral readouts (Glover, 2012), which are significantly faster than EPI for given gradient specifications. Another example is matched-filter EPI, which offers enhanced SNR efficiency when spatial filtering is involved in data post-processing (Kasper et al., 2014). Regarding field fluctuations, each such alternative will give rise to different hardware-related effects and translate fluctuations into different artifacts. Importantly, upon deviation from regular EPI, artifacts arising from slow field fluctuations will no longer amount to mere shifts and distortions and can thus no longer be addressed by co-registration. Likewise, the concept of calibration echo trains has no generalization for trajectories that are not repetitive in themselves. Thus, of the correction approaches surveyed here the only generally applicable ones will be those based on navigators, covering slow fluctuations, and external field probes for full field information.

A third perspective naturally concerned by issues of field stability is

phase-based BOLD analysis (Bianciardi et al., 2014, 2009; Hagberg et al., 2008). Commonly, image processing in fMRI is limited to magnitude images, discarding the image phase because it is inherently more sensitive to field fluctuations. It is also more susceptible to ghosting, which the magnitude operation masks when it occurs out-of-phase with properly depicted signal (Fig. 5). Nevertheless, due to its very sensitivity to subtle field changes the phase of fMRI data is also a carrier of BOLD information. Fully deploying this information requires particularly accurate fluctuation correction, which would equally advance derived phase-based contrasts such as functional quantitative susceptibility (Liu et al., 2015; Ozbay et al., 2016), especially at high field.

The advanced scenarios discussed in this section all explore ways of enhancing the performance of fMRI while also boosting challenges related to field fluctuations, be it in the form of larger field excursions, greater sensitivity to them, or greater difficulty of correction. This observation suggests two conclusions. One is that magnetic field imperfections of various sorts, while of moderate impact in the present study, will tend to play an increasing role as fMRI advances. The other conclusion is that the ability to record spatiotemporal field evolution in the first place is pivotal, should be versatile, and should not interfere with sequence design, which speaks in favor of dedicated field sensors.

5. Conclusion

According to the results of this work long-range field fluctuations are a relevant confound in fMRI. Field fluctuations of physiological origin are predominantly due to breathing and small relative to both hardware-related field effects and image fluctuations of other physiological causes. In a standard fMRI protocol at 3 T full field correction at the image reconstruction stage afforded SFNR gains on the order of 67% and 6%, respectively, without and with complementary image realignment. Based on the presented analysis of fluctuation contributions the advantage of full field correction is anticipated to increase with field strength, upon phase-sensitive BOLD analysis, and with non-Cartesian readouts, for which even slow field fluctuations cannot be addressed by image realignment.

Acknowledgments

Technical support from Philips Healthcare, Best, The Netherlands, is gratefully acknowledged. This work has been funded, in part, by the NCCR Neural Plasticity and Repair at ETH Zurich and University of Zurich (LK, KES, KPP), the René and Susanne Braginsky Foundation (KES), FP7 Marie Curie International Fellowship and University of Zurich Forschungskredit (AOD), and the University of Zurich (KPP, KES).

Appendix A. Supplementary material

Supplementary material associated with this article can be found in the online version at doi:10.1016/j.neuroimage.2017.01.014.

References

Alhamud, A., Taylor, P.A., van der Kouwe, A.J.W., Meintjes, E.M., 2016. Real-time measurement and correction of both B_0 changes and subject motion in diffusion tensor imaging using a double volumetric navigated (DvNav) sequence. NeuroImage 126, 60–71. http://dx.doi.org/10.1016/j.neuroimage.2015.11.022.

Andersson, J.L.R., Hutton, C., Ashburner, J., Turner, R., Friston, K., 2001. Modeling geometric deformations in EPI time series. NeuroImage 13, 903–919. http://dx.doi.org/10.1006/nimg.2001.0746.

Andersson, J.L.R., Skare, S., Ashburner, J., 2003. How to correct susceptibility distortions in spin-echo echo-planar images: application to diffusion tensor imaging. NeuroImage 20, 870–888. http://dx.doi.org/10.1016/S1053-8119(03)00336-7.

Ashburner, J., Friston, K., 2007. Chapter 4 - rigid body registration. In: Friston, K., Ashburner, J., Kiebel, S., Nichols, T., Penny, W. (Eds.), Statistical Parametric Mapping: The Analysis of Funtional Brain Images. Elsevier/Academic Press, Amsterdam, Boston, 49–62.

Ashburner, J., Friston, K.J., 2005. Unified segmentation. NeuroImage 26, 839–851. http://dx.doi.org/10.1016/j.neuroimage.2005.02.018.

Bandettini, P.A., Wong, E.C., Hinks, R.S., Tikofsky, R.S., Hyde, J.S., 1992. Time course EPI of human brain function during task activation. Magn. Reson. Med. 25, 390–397.

Barmet, C., De Zanche, N., Wilm, B.J., Pruessmann, K.P., 2009. A transmit/receive system for magnetic field monitoring of in vivo MRI. Magn. Reson. Med. 62, 269–276. http://dx.doi.org/10.1002/mrm.21996.

Barmet, C., Wilm, B.J., Pavan, M., Katsikatsos, G., Keupp, J., Mens, G., Pruessmann, K.P., 2010. Concurrent higher-order field monitoring for routine head MRI: an integrated heteronuclear setup. Proc. Int. Soc. Magn. Reson. Med. 18, 216.

Barmet, C., Zanche, N.D., Pruessmann, K.P., 2008. Spatiotemporal magnetic field monitoring for MR. Magn. Reson. Med. 60, 187–197. http://dx.doi.org/10.1002/mrm.21603.

Bartlett, M., 1948. Smoothing periodograms from time-series with continuous spectra. Nature 161, 686–687.

Beatty, P.J., Nishimura, D.G., Pauly, J.M., 2005. Rapid gridding reconstruction with a minimal oversampling ratio. IEEE Trans. Med. Imaging 24, 799–808. http://dx.doi.org/10.1109/TMI.2005.848376.

Bianciardi, M., Fukunaga, M., van Gelderen, P., Horovitz, S.G., de Zwart, J.A., Shmueli, K., Duyn, J.H., 2009. Sources of functional magnetic resonance imaging signal fluctuations in the human brain at rest: a 7 T study. Magn. Reson. Imaging 27, 1019–1029. http://dx.doi.org/10.1016/j.mri.2009.02.004.

Bianciardi, M., van Gelderen, P., Duyn, J.H., 2014. Investigation of BOLD fMRI resonance frequency shifts and quantitative susceptibility changes at 7 T. Hum. Brain Mapp. 35, 2191–2205. http://dx.doi.org/10.1002/hbm.22320.

Birn, R.M., Diamond, J.B., Smith, M.A., Bandettini, P.A., 2006. Separating respiratory-variation-related neuronal-activity-related fluctuations in fluctuations from fMRI. Neuroimage 31, 1536–1548. http://dx.doi.org/10.1016/j.neuroimage.2006.02.048.

Bruder, H., Fischer, H., Reinfelder, H.-E., Schmitt, F., 1992. Image reconstruction for echo planar imaging with nonequidistant k-space sampling. Magn. Reson. Med. 23, 311–323.

Busch, J., Vannesjo, S.J., Barmet, C., Pruessmann, K.P., Kozerke, S., 2014. Analysis of temperature dependence of background phase errors in phase-contrast magnetic resonance imaging. J. Cardiovasc. Magn. Reson. 16, 97. http://dx.doi.org/10.1186/s12968-014-0097-6.

Calhoun, V.D., Adalı, T., Pearlson, G.D., Van Zijl, P.C.M., Pekar, J.J., 2002. Independent component analysis of fMRI data in the complex domain. Magn. Reson. Med. 48, 180–192.

Chang, C., Glover, G.H., 2009. Relationship between respiration, end-tidal CO2, and BOLD signals in resting-state fMRI. NeuroImage 47, 1381–1393. http://dx.doi.org/10.1016/j.neuroimage.2009.04.048.

Chang, C., Cunningham, J.P., Glover, G.H., 2009. Influence of heart rate on the BOLD signal: The cardiac response function. NeuroImage 44, 857–869. http://dx.doi.org/10.1016/j.neuroimage.2008.09.029.

De Zanche, N., Barmet, C., Nordmeyer-Massner, J.A., Pruessmann, K.P., 2008. NMR probes for measuring magnetic fields and field dynamics in MR systems. Magn. Reson. Med. 60, 176–186. http://dx.doi.org/10.1002/mrm.21624.

Diaconescu, A.O., Mathys, C., Weber, L.A.E., Daunizeau, J., Kasper, L., Lomakina, E.I., Fehr, E., Stephan, K.E., 2014. Inferring on the intentions of others by hierarchical bayesian learning. PLoS Comput. Biol. 10, e1003810. http://dx.doi.org/10.1371/journal.pcbi.1003810.

Diaconescu, A.O., Mathys, C.D., Weber, L.A.E., Kasper, L., Mauer, J., Stephan, K.E., 2016. Hierarchical prediction errors in midbrain and septum during social learning. Soc. Cogn. Affect Neurosci. http://dx.doi.org/10.1093/scan/nsw171, (in press).

Dietrich, B.E., Brunner, D.O., Wilm, B.J., Barmet, C., Pruessmann, K.P., 2016. Continuous magnetic field monitoring using rapid re-excitation of NMR probe sets. IEEE Trans. Med. Imaging 35, 1452–1462. http://dx.doi.org/10.1109/TMI.2016.2514608.

Duerst, Y., Wilm, B.J., Dietrich, B.E., Vannesjo, S.J., Barmet, C., Schmid, T., Brunner, D.O., Pruessmann, K.P., 2015. Real-time feedback for spatiotemporal field stabilization in MR systems. Magn. Reson. Med. 73, 884–893. http://dx.doi.org/10.1002/mrm.25167.

Duerst, Y., Wilm, B.J., Wyss, M., Dietrich, B.E., Gross, S., Schmid, T., Brunner, D.O., Pruessmann, K.P., 2016. Utility of real-time field control in T2*-weighted head MRI at 7 T. Magn. Reson. Med. 76, 430–439. http://dx.doi.org/10.1002/mrm.25838.

El-Sharkawy, A.M., Schär, M., Bottomley, P.A., Atalar, E., 2006. Monitoring and correcting spatio-temporal variations of the MR scanner's static magnetic field. Magn. Reson. Mater. Phys. Biol. Med. 19, 223–236.

Foerster, B.U., Tomasi, D., Caparelli, E.C., 2005. Magnetic field shift due to mechanical vibration in functional magnetic resonance imaging. Magn. Reson. Med. 54, 1261–1267. http://dx.doi.org/10.1002/mrm.20695.

Frackowiak, R.S., Heather, J.D., Poline, J.-B., Frith, C.D., Ashburner, J., Friston, K.J., 1995. Spatial registration and normalization of images. Hum. Brain Mapp. 3, 165–189. http://dx.doi.org/10.1002/hbm.460030303.

Friedman, L., Glover, G.H., 2006. Report on a multicenter fMRI quality assurance protocol. J. Magn. Reson. Imaging 23, 827–839. http://dx.doi.org/10.1002/jmri.20583.

Giannelli, M., Diciotti, S., Tessa, C., Mascalchi, M., 2010. Effect of echo spacing and readout bandwidth on basic performances of EPI-fMRI acquisition sequences implemented on two 1.5 T MR scanner systems. Med. Phys. 37, 303–310.

Glover, G.H., 2012. Spiral imaging in fMRI. NeuroImage 62, 706–712. http://dx.doi.org/10.1016/j.neuroimage.2011.10.039.

Glover, G.H., Li, T.Q., Ress, D., 2000. Image-based method for retrospective correction of physiological motion effects in fMRI: RETROICOR. Magn. Reson. Med. 44, 162–167 . http://dx.doi.org/10.1002/1522-2594(200007)44:1 < 162::AID-MRM23 >

3.0.CO;2-E.
Gross, S., Barmet, C., Dietrich, B.E., Brunner, D.O., Schmid, T., Pruessmann, K.P., 2016. Dynamic nuclear magnetic resonance field sensing with part-per-trillion resolution. Nat. Commun. 7 (2016), 13702. http://dx.doi.org/10.1038/ncomms13702.
Hagberg, G.E., Bianciardi, M., Brainovich, V., Cassarà, A.M., Maraviglia, B., 2008. The effect of physiological noise in phase functional magnetic resonance imaging: from blood oxygen level-dependent effects to direct detection of neuronal currents. Magn. Reson. Imaging 26, 1026–1040. http://dx.doi.org/10.1016/j.mri.2008.01.010.
Harvey, A.K., Pattinson, K.T.S., Brooks, J.C.W., Mayhew, S.D., Jenkinson, M., Wise, R.G., 2008. Brainstem functional magnetic resonance imaging: disentangling signal from physiological noise. J. Magn. Reson. Imaging 28, 1337–1344. http://dx.doi.org/10.1002/jmri.21623.
Hennel, F., 1997. Multiple-shot echo-planar imaging. Concepts Magn. Reson. 9, 43–58. http://dx.doi.org/10.1002/(SICI)1099-0534(1997)9:1 < 43::AID-CMR4 > 3.0.CO;2-N.
Henry, P.-G., Van de Moortele, P.-F., Giacomini, E., Nauerth, A., Bloch, G., 1999. Field-frequency locked in vivo proton MRS on a whole-body spectrometer. Magn. Reson. Med. 42, 636–642.
Hinks, R.S., Frigo, F.J., Mock, B.J., Zhao, X., Sangill, R., Collick, B.D., 2006. Image reconstruction using dynamic EPI phase correction. Proc. Intl. Soc. Mag. Reson. Med. 14, 2348.
Hu, X., Kim, S.-G., 1994. Reduction of signal fluctuation in functional MRI using navigator echoes. Magn. Reson. Med. 31, 495–503.
Jackson, J.I., Meyer, C.H., Nishimura, D.G., Macovski, A., 1991. Selection of a convolution function for Fourier inversion using gridding (computerised tomography application). IEEE Trans. Med. Imaging 10, 473–478. http://dx.doi.org/10.1109/42.97598.
Juchem, C., Nixon, T.W., Diduch, P., Rothman, D.L., Starewicz, P., De Graaf, R.A., 2010. Dynamic shimming of the human brain at 7 T. Concepts Magn. Reson. Part B: Magn. Reson. Eng. 37B, 116–128. http://dx.doi.org/10.1002/cmr.b.20169.
Kasper, L., Bollmann, S., Diaconescu, A.O., Hutton, C., Heinzle, J., Iglesias, S., Hauser, T.U., Sebold, M., Manjaly, Z.-M., Pruessmann, K.P., Stephan, K.E., 2017. The PhysIO Toolbox for modeling physiological noise in fMRI data. J. Neurosci. Methods 276, 56–72. http://dx.doi.org/10.1016/j.jneumeth.2016.10.019.
Kasper, L., Bollmann, S., Vannesjo, S.J., Gross, S., Haeberlin, M., Dietrich, B.E., Pruessmann, K.P., 2015. Monitoring, analysis, and correction of magnetic field fluctuations in echo planar imaging time series. Magn. Reson. Med. 74, 396–409. http://dx.doi.org/10.1002/mrm.25407.
Kasper, L., Haeberlin, M., Dietrich, B.E., Gross, S., Barmet, C., Wilm, B.J., Vannesjo, S.J., Brunner, D.O., Ruff, C.C., Stephan, K.E., Pruessmann, K.P., 2014. Matched-filter acquisition for BOLD fMRI. NeuroImage 100, 145–160. http://dx.doi.org/10.1016/j.neuroimage.2014.05.024.
Liu, C., Li, W., Tong, K.A., Yeom, K.W., Kuzminski, S., 2015. Susceptibility-weighted imaging and quantitative susceptibility mapping in the brain. J. Magn. Reson. Imaging 42, 23–41. http://dx.doi.org/10.1002/jmri.24768.
Liu, H.-L., Kochunov, P., Lancaster, J.L., Fox, P.T., Gao, J.-H., 2001. Comparison of navigator echo and centroid corrections of image displacement induced by static magnetic field drift on echo planar functional MRI. J. Magn. Reson. Imaging 13, 308–312.
Mandeep, S.D., Ingeholm, J.E., Haxby, J.V., 1999. Localization of cardiac-induced signal change in fMRI. NeuroImage 9, 407–415. http://dx.doi.org/10.1006/nimg.1998.0424.
Mansfield, P., 1977. Multi-planar image formation using NMR spin echoes. J. Phys. C: Solid State Phys. 10. http://dx.doi.org/10.1088/0022-3719/10/3/004.
Murphy, K., Birn, R.M., Bandettini, P.A., 2013. Resting-state fMRI confounds and cleanup. NeuroImage 80, 349–359. http://dx.doi.org/10.1016/j.neuroimage.2013.04.001.
Ozbay, P.S., Warnock, G., Rossi, C., Kuhn, F., Akin, B., Pruessmann, K.P., Nanz, D., 2016. Probing neuronal activation by functional quantitative susceptibility mapping under a visual paradigm: a group level comparison with BOLD fMRI and PET. NeuroImage 137, 52–60. http://dx.doi.org/10.1016/j.neuroimage.2016.05.013.
Ogawa, S., Lee, T.M., Kay, A.R., Tank, D.W., 1990. Brain magnetic resonance imaging with contrast dependent on blood oxygenation. Proc. Natl. Acad. Sci. USA 87, 9868–9872.
Pearson, K., 1901. On lines and planes of closest fit to systems of points in space. Philos. Mag. 2, 559–572.
Pfeuffer, J., Van de Moortele, P.-F., Ugurbil, K., Hu, X., Glover, G.H., 2002. Correction of physiologically induced global off-resonance effects in dynamic echo-planar and spiral functional imaging. Magn. Reson. Med. 47, 344–353.
Power, J.D., Barnes, K.A., Snyder, A.Z., Schlaggar, B.L., Petersen, S.E., 2012. Spurious but systematic correlations in functional connectivity MRI networks arise from subject motion. NeuroImage 59, 2142–2154. http://dx.doi.org/10.1016/j.neuroimage.2011.10.018.
Pruessmann, K.P., Dietrich, B.E., Barmet, C., 2011. Observation of cardiovascular dynamics by field recording with an NMR probe. Proc. Intl. Soc. Mag. Reson. Med. 19, 1171.
Pruessmann, K.P., Weiger, M., Börnert, P., Boesiger, P., 2001. Advances in sensitivity encoding with arbitrary k-space trajectories. Magn. Reson. Med. 46, 638–651. http://dx.doi.org/10.1002/mrm.1241.
Raj, D., Paley, D.P., Anderson, A.W., Kennan, R.P., Gore, J.C., 2000. A model for susceptibility artefacts from respiration in functional echo-planar magnetic resonance imaging. Phys. Med. Biol. 45, 3809–3820.
Rowe, D.B., 2005. Parameter estimation in the magnitude-only and complex-valued fMRI data models. NeuroImage 25, 1124–1132. http://dx.doi.org/10.1016/j.neuroimage.2004.12.048.
Rowe, D.B., Logan, B.R., 2004. A complex way to compute fMRI activation. NeuroImage 23, 1078–1092. http://dx.doi.org/10.1016/j.neuroimage.2004.06.042.
Salimi-Khorshidi, G., Douaud, G., Beckmann, C.F., Glasser, M.F., Griffanti, L., Smith, S.M., 2014. Automatic denoising of functional MRI data: combining independent component analysis and hierarchical fusion of classifiers. NeuroImage 90, 449–468. http://dx.doi.org/10.1016/j.neuroimage.2013.11.046.
Schmitt, F., Stehling, M.K., Turner, R., 1998. Echo-Planar Imaging Theory, Technique and Application. Springer Berlin Heidelberg.
Sengupta, S., Welch, E.B., Zhao, Y., Foxall, D., Starewicz, P., Anderson, A.W., Gore, J.C., Avison, M.J., 2011. Dynamic B_0 shimming at 7 T. Magn. Reson. Imaging 29, 483–496. http://dx.doi.org/10.1016/j.mri.2011.01.002.
Splitthoff, D.N., Testud, F., Hennig, J., Speck, O., Zaitsev, M., 2007. Real-time prospective shim correction using self-referencing navigators. Proc. Int. Soc. Mag. Reson. Med. 15, 985.
Splitthoff, D.N., Zaitsev, M., 2009. SENSE shimming (SSH): a fast approach for determining B_0 field inhomogeneities using sensitivity coding. Magn. Reson. Med. 62, 1319–1325. http://dx.doi.org/10.1002/mrm.22083.
Van de Moortele, P.-F., Pfeuffer, J., Glover, G.H., Ugurbil, K., Hu, X., 2002. Respiration-induced B_0 fluctuations and their spatial distribution in the human brain at 7 Tesla. Magn. Reson. Med. 47, 888–895. http://dx.doi.org/10.1002/mrm.10145.
van Gelderen, P., de Zwart, J.A., Starewicz, P., Hinks, R.S., Duyn, J.H., 2007. Real-time shimming to compensate for respiration-induced B_0 fluctuations. Magn. Reson. Med. 57, 362–368. http://dx.doi.org/10.1002/mrm.21136.
Vannesjo, S.J., Dietrich, B.E., Pavan, M., Brunner, D.O., Wilm, B.J., Barmet, C., Pruessmann, K.P., 2014. Field camera measurements of gradient and shim impulse responses using frequency sweeps. Magn. Reson. Med. 72, 570–583. http://dx.doi.org/10.1002/mrm.24934.
Vannesjo, S.J., Wilm, B.J., Duerst, Y., Gross, S., Brunner, D.O., Dietrich, B.E., Schmid, T., Barmet, C., Pruessmann, K.P., 2015. Retrospective correction of physiological field fluctuations in high-field brain MRI using concurrent field monitoring. Magn. Reson. Med. 73, 1833–1843. http://dx.doi.org/10.1002/mrm.25303.
Vannesjo, S.J., Graedel, N.N., Kasper, L., Gross, S., Busch, J., Haeberlin, M., Barmet, C., Pruessmann, K.P., 2016a. Image reconstruction using a gradient impulse response model for trajectory prediction. Magn. Reson. Med. 76, 45–58. http://dx.doi.org/10.1002/mrm.25841.
Vannesjo, S.J., Duerst, Y., Vionnet, L., Dietrich, B.E., Pavan, M., Gross, S., Barmet, C., Pruessmann, K.P., 2016b. Gradient and shim pre-emphasis by inversion of a linear time-invariant system model. Magn. Reson. Med.. http://dx.doi.org/10.1002/mrm.26531, (published ahead of print).
Versluis, M.J., Peeters, J.M., van Rooden, S., van der Grond, J., van Buchem, M.A., Webb, A.G., van Osch, M.J.P., 2010. Origin and reduction of motion and f0 artifacts in high resolution T2*-weighted magnetic resonance imaging: application in Alzheimer's disease patients. NeuroImage 51, 1082–1088. http://dx.doi.org/10.1016/j.neuroimage.2010.03.048.
Ward, H.A., Riederer, S.J., Jack, C.R., 2002. Real-time autoshimming for echo planar timecourse imaging. Magn. Reson. Med. 48, 771–780. http://dx.doi.org/10.1002/mrm.10259.
Welvaert, M., Rosseel, Y., 2013. On the definition of signal-to-noise ratio and contrast-to-noise ratio for fMRI data. PLoS ONE 8, e77089. http://dx.doi.org/10.1371/journal.pone.0077089.
Wilm, B.J., Barmet, C., Pavan, M., Pruessmann, K.P., 2011. Higher order reconstruction for MRI in the presence of spatiotemporal field perturbations. Magn. Reson. Med. 65, 1690–1701. http://dx.doi.org/10.1002/mrm.22767.
Wilm, B.J., Nagy, Z., Barmet, C., Vannesjo, S.J., Kasper, L., Haeberlin, M., Gross, S., Dietrich, B.E., Brunner, D.O., Schmid, T., Pruessmann, K.P., 2015. Diffusion MRI with concurrent magnetic field monitoring. Magn. Reson. Med. 74, 925–933. http://dx.doi.org/10.1002/mrm.25827.
Windischberger, C., Langenberger, H., Sycha, T., Tschernko, E.M., Fuchsjäger-Mayerl, G., Schmetterer, L., Moser, E., 2002. On the origin of respiratory artifacts in BOLD-EPI of the human brain. Magn. Reson. Imaging 20, 575–582. http://dx.doi.org/10.1016/S0730-725X(02)00563-5.